Doctoral

Engineering

2018

Label-Free Discrimination Analysis of De-Differentiated Vascular Smooth Muscle Cells, Mesenchymal Stem Cells and Their Vascular and Osteogenic Progeny Using Vibrational Spectroscopy

Claire Moloney
Dublin City University, Dublin

Jennifer McIntyre
Technological University Dublin, jennifer.mcintyre@tudublin.ie

Adrian Maguire
Dublin Institute of Technology, adrian.maguire@mydit.ie

See next page for additional authors

Authors

Claire Moloney, Jennifer McIntyre, Adrian Maguire, Roya Hakimjavadi, Denise Burtenshaw, Gillian Casey, Mariana Di Luca, Mariana Di Luca, Bryan Hennelly, Hugh Byrne, and Paul A. Cahill

Label-free discrimination analysis of de-differentiated vascular smooth muscle cells, mesenchymal stem cells and their vascular and osteogenic progeny using vibrational spectroscopy

Claire Molony[a], Jennifer McIntyre[b], Adrian Maguire[b], Roya Hakimjavadi[a], Denise Burtenshaw[a], Gillian Casey[a], Mariana Di Luca[a], Bryan Hennelly[c,1], Hugh J. Byrne[b,1], Paul A. Cahill[a,*]

[a] Dublin City University, Vascular Biology & Therapeutics, School of Biotechnology, Dublin, Ireland
[b] Dublin Institute of Technology, FOCAS Research Institute, Dublin, Ireland
[c] National University of Ireland, Maynooth, Department of Electronic Engineering and Department of Computer Science, Kildare, Ireland

ARTICLE INFO

ABSTRACT

The accumulation of vascular smooth muscle (SMC)-like cells and stem cell-derived myogenic and osteogenic progeny contributes significantly to arteriosclerotic disease. This study established whether label-free vibrational spectroscopy can discriminate de-differentiated 'synthetic' SMCs from undifferentiated stem cells and their myogenic and osteogenic progeny in vitro, compared with conventional immunocytochemical and genetic analyses. TGF-β1- and Jagged1-induced myogenic differentiation of CD44$^+$ mesenchymal stem cells was confirmed in vitro by immunocytochemical analysis of specific SMC differentiation marker expression (α-actin, calponin and myosin heavy chain 11), an epigenetic histone mark (H3K4me2) at the myosin heavy chain 11 locus, promoter transactivation and mRNA transcript levels. Osteogenic differentiation was confirmed by alizarin red staining of calcium deposition. Fourier Transform Infrared (FTIR) maps facilitated initial screening and discrimination while Raman spectroscopy of individual cell nuclei revealed specific spectral signatures of each cell type in vitro, using Principal Components Analysis (PCA). PCA fed Linear Discriminant Analysis (LDA) enabled quantification of this discrimination and the sensitivity and specificity value was determined for all cell populations based on a leave-one-out cross validation method and revealed that de-differentiated SMCs and stem-cell derived myogenic progeny in culture shared the greatest similarity. FTIR and Raman spectroscopy discriminated undifferentiated stem cells from both their myogenic and osteogenic progeny. The ability to detect stem cell-derived myogenic progeny using label-free platforms in situ may facilitate interrogation of these important phenotypes during vascular disease progression.

1. Introduction

Cardiovascular diseases (CVD), such as arteriosclerosis, in-stent restenosis and pulmonary hypertension (PAH), remain a leading cause of global death and result from pathologic arterial remodelling [1,2]. A hallmark of arterial remodelling is intimal medial thickening (IMT) due to the accumulation of vascular smooth muscle (SMC)-like cells within the intima leading to the obstruction of blood flow and resulting in a heart attack or stroke [3]. The source of these neointimal cells includes stem cell-derived myogenic progeny (St-SMCs) [4–7] and SMCs following endothelial-mesenchymal transition (EndMT) [4,8] in addition to de-differentiation and reprogramming of SMCs (ddSMCs) [9]. Transforming growth factor (TGF)-β1 and Notch ligands (Jagged1) are

both putative regulators of stem cell myogenic differentiation in vitro [10,11] and may contribute to stem cell myogenic differentiation and SMC accumulation during arterial remodelling in vivo [6,12,13]. Therefore, early detection of de-differentiated SMCs and/or stem cell-derived progeny (following myogenic differentiation) by these factors as a source of neointimal cells during early stages of disease and its progression by means a novel photonic interrogation system would be highly desirable.

Amongst the various imaging platforms available to interrogate closely related cell populations and discriminate cell-dependent changes in vessel structure due to arteriosclerosis, label-free techniques such as vibrational spectroscopy have shown great promise [14]. Vibrational spectroscopy is a subset of spectroscopy which analyses

vibrations within a molecule (or material), which are characteristic of the molecular structure and, in polyatomic molecules, give rise to a spectroscopic "fingerprint" of that molecule. The spectrum of vibrational energies can thus be employed to characterise a molecular structure, or changes to it due to the local environment or external factors (*e.g.* radiation, chemical agents). Vibrational energies fall within the mid - Infrared (IR) region of the electromagnetic spectrum and are commonly probed through IR absorption spectroscopy [15]. Raman spectroscopy is a complementary technique whereby incident radiation couples with the oscillating polarisation of the molecule and thus generates or annihilates a vibrational quantum, similarly resulting in a vibrational spectrum [16]. The differing underlying mechanisms give rise to a complementarity of the two techniques, such that vibrations of asymmetric, polar bonds tend to be strong in IR spectra, whereas Raman is particularly suitable as a probe of symmetric, nonpolar groups. Moreover, FTIR monitors the absorption of IR radiation whereas Raman scattering can be employed in the UV, visible or near-IR regions of the spectrum and thus offers intrinsically higher spatial resolution for cellular and subcellular mapping or profiling. The limit of resolution is determined classically by the wavelength ($< 1\,\mu m$ for Raman, $\sim 5\text{-}10\,\mu m$ for IR) [17]. Therefore, the longer wavelength of mid infrared radiation, coupled with the use of multidetector arrays in the Fourier Transform mode, render IR techniques more suitable for mapping larger cell populations or tissue sections [18].

The current study was undertaken to establish whether vibrational spectroscopy could be implemented as a novel photonic platform to discriminate undifferentiated bone marrow-derived stem cells from their myogenic progeny following differentiation *in vitro* and further whether these cell populations could be discriminated from de-differentiated 'synthetic' SMCs and stem cell-derived osteogenic progeny.

2. Methods

2.1. Materials

Unless otherwise stated, all chemicals and reagents were obtained from Sigma-Aldrich and were of the highest purity commercially available (Sigma-Aldrich, Ireland). A more detailed version of the Methods is presented in the Appendix A.

2.2. Cell culture

Freshly isolated vascular SMC were grown up to passage 4 in culture in RPMI-1640 supplemented with 10% FCS, as previously described [19] and were deemed proliferative de-differentiated "synthetic" SMCs (ddSMCs). Sprague-Dawley rat mesenchymal stem cells (bm-MSC) were purchased from Gibco (S1601-100) and cultured as per the manufacturer's instructions. These rat bm-MSCs have been validated previously as multipotent stem cells that have a large capacity for self-renewal while maintaining their multipotency [20,21]. Importantly, this cell population expresses all the common MSC markers and is able to differentiate into the three lineages recapitulating a 'true' mesenchymal cell phenotype http://tools.thermofisher.com/content/sfs/manuals/GIBCO_Rat_(SD)_MSCs.pdf. Myogenic and osteogenic differentiation of bm-MSC was established following culture of cells in DMEM supplemented with TGF-β1 (R&D, 7666-MB-005) (St-SMC-TGF-β1), recombinant Jagged1-Fc (R&D, 599-JG) (St-SMC-Jag-1) for 14 days and StemPro® Osteogenic Differentiation Kit (ThermoFisher, USA, A1007201) for 21 days, respectively.

2.3. Immunocytochemistry

Fixed cells were incubated overnight at 4 °C with primary antibodies at the appropriate dilution washed and further incubated with the secondary antibody (Biosciences, anti-goat A-11055, anti-rabbit A11008) at a dilution of 1:1000 for 1 h at room temperature. An Olympus CK30 microscope with CellˆF software was used to capture images. At least five images from the Olympus CK30 microscopy per experimental group (minimum n = 3) were analysed using ImageJ software as previously described [20,21].

2.4. Realtime qRT-PCR

Quantitative real-time RT-PCR was performed using the Rotor Gene (RG-3000, Corbett Research) and a Quantitect™ Primer assay system using Quantitect rat primers (Qiagen, Manchester UK) as previously described [20]. Gene expression was normalised to that of the housekeeping gene, hypoxanthine-guanine phosphoribosyltransferase (HPRT).

2.5. Chromatin immunoprecipitation assay (ChIP assay)

Cells were cross-linked and DNA was sheared to 500–1000 bp by sonication before ChIP analysis was carried out using the MAGnify™ Chromatin Immunoprecipitation System (InVitrogen, Bioscience Ireland, cat no 49-2024) according to the manufacturer's instruction. Recovered DNA was analysed by qPCR. The ChIP-qPCR data was normalised for sources of variability, including amount of chromatin, efficiency of immunoprecipitation, and DNA recovery using the Fold Enrichment Method. This normalisation method is also called 'signal over background' or 'relative to the no-antibody control'. With this method, the ChIP signals are divided by the no-antibody signals, representing the ChIP signal as the fold increase in signal relative to the background signal. The assumption of this method is that the level of background signal is reproducible between different primer sets, samples, and replicate experiments. All samples were performed in triplicate from at least three independent experiments.

2.6. Myh11-promoter luciferase assay

Cells were transiently transfected with Myh11 reporter plasmid (Myh11-GLuc, GeneCopoeia, Inc. Cat No; MPRM16957-PG02) and Renilla reporter plasmid (Promega, Madison, WI) for 24 h using TransIT-X2® Dynamic Delivery System (Mirus Bio, Madison, WI) in OptiMEM according to the manufacturer's instruction. Gaussia luciferase activities were normalised to the activity of internal control Renilla luciferase activities using the dual luciferase assay system described by the manufacturer (Promega, Madison, WI). All assays were performed in triplicate.

2.7. Sample preparation for spectroscopic analysis

For both FTIR and Raman spectroscopic analyses, cells were seeded on calcium fluoride slides in 6 well plates at approximately 10,000 cells/well. After fixation, the slides were washed with PBS and placed briefly in distilled water. The slides were left to air dry before recording spectra.

2.8. FTIR spectroscopy

IR absorption measurements were carried out using a Perkin Elmer Spotlight 400 N FTIR imaging system. The system was equipped with an AutoImage microscope system operating with a × 40 Cassegrain objective and operates in transmission or reflection mode. FTIR images were acquired in transmission mode with 10 scans of a $150 \times 150\,\mu m$ area of the slide for each cell population. All experiments were carried out in triplicate (576 spectra per scan were recorded, 30 scans per sample, $\sim 15,000$ spectra per cell population). Individual spectra were acquired with a liquid nitrogen cooled mercury cadmium telluride (MCT-A) line detector of pixel size $6.25\,\mu m \times 6.25\,\mu m$ at a spectral resolution of $4\,cm^{-1}$, interferometer speed of 1.0 cm/s and the useable spectral range is restricted to $900\text{–}4000\,cm^{-1}$. Background

measurements were acquired on a region with no cells with 120 scans per pixel whereas 32 scans per pixel were recorded from the sample.

2.9. Raman spectroscopy

Raman spectra were recorded using a custom-built Raman microspectroscopy system, as previously described [22,23]. Briefly, this system employed a 150 mW laser with a wavelength of 532 nm (Laser Quantum, Torus), spectrograph (Andor, Shamrock 500) operating with 600 lines/mm grating, and a CCD camera (Andor; DU420A-BR-DD) cooled to − 80 °C. A 50 × microscope objective (MO), with numerical aperture of 0.8 (Olympus, UMPlanFl), was used to image the spectral irradiance to a 100 μm confocal aperture, which isolates the signal from the cell nucleus, and minimises background noise from the sample substrate, as well as from optical elements in the system [22,23].

2.10. Data processing and analysis

The different data pre-processing and analysis steps were performed using Matlab (Mathworks, USA). For FTIR data, the resonant Mie scattering correction algorithm (RMieS-EMSC) was employed to remove scattering effects from FTIR spectra [24], as has been successfully demonstrated in a number of studies [25]. For Raman data, cosmic ray removal is followed by application of an extended multiplicative signal correction (EMSC) algorithm as described in detail previously [23]. After pre-processing, Principal Components Analysis (PCA) was employed as an unsupervised multivariate analysis tool to differentiate the data recorded from different cell phenotypes.

2.11. Statistical analysis

All biochemical analysis experiments were performed in triplicate and data are presented as mean ± SEM for at least three independent runs. Statistical analysis was performed with Prism v6 software package using t-test for parametric data or a Wilcoxon Signed Rank test for non-parametric data.

3. Results

3.1. FTIR and Raman spectroscopy both discriminate bone-marrow derived mesenchymal stem cells from their osteogenic progeny in vitro

A sample population of CD44$^+$ bm-MSCs was analysed by both FTIR and Raman spectroscopy, and the raw spectra recorded, processed and the mean spectrum presented [Fig. 1]. The FTIR bands are labelled with assignments of typical biochemical origin. In the "high wavenumber region", > 2500 cm^{-1}, the distinctive vibrations of N−H, C−H and O−H of lipids and proteins can be found, whereas in the "fingerprint region", < 2000 cm^{-1}, the features are typically more complex combinations, including the Amide I (1650 cm^{-1}) and Amide II (1520 cm^{-1}) modes of proteins, nucleic acid phosphate stretching modes at 1070 cm^{-1} and 1250 cm^{-1} and lipidic derived features at 1310 cm^{-1} and 1750 cm^{-1}. A more detailed list of band assignments is provided in Table 1. Mean Raman spectra for bm-MSC nuclei were also recorded and analysed following cosmic ray removal and EMSC correction. The prominent peaks in bm-MSCs are annotated and presented in Fig. 1(b), Table 2. It should be noted that, although complementary techniques, the features in the respective spectra of FTIR and Raman have similar origin. Thus, the Raman spectrum of the nucleus exhibits similarly prominent signatures associated with proteins and lipids across the fingerprint region, as well as large peaks related to DNA and RNA at 785 cm^{-1}.

Osteogenic differentiation of bm-MSC to osteogenic progeny (St-Osteo) was first validated by phase contrast microscopy of gross morphological differences before and after osteogenic differentiation. St-Osteo cells were morphologically distinct from bm-MSC and exhibited a
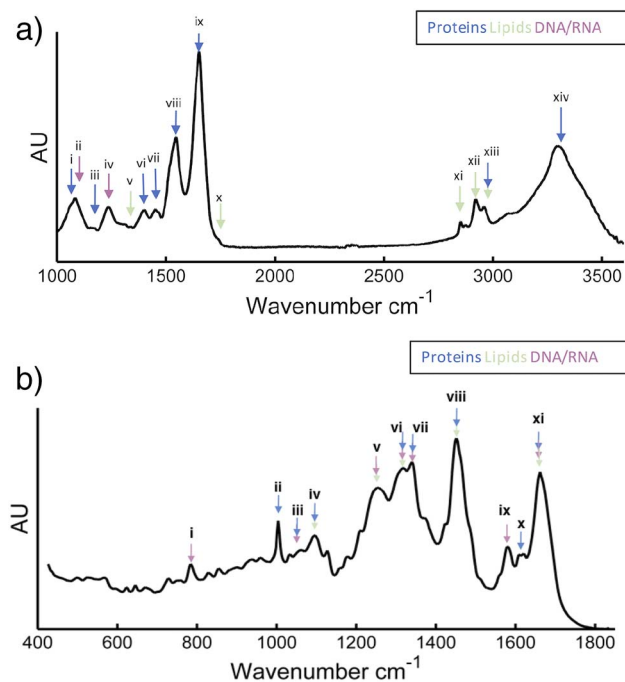

Fig. 1. (a). Representative mean FTIR spectra recorded for bm-MSCs following Resonant Mie (RMieS) correction with classification of relevant peaks and their known association to proteins, nucleic acid and lipids described in Table 1. (b) Processed mean Raman spectra for bm-MSCs following cosmic ray removal and EMSC correction and their known association to proteins, nucleic acid and lipids are described in Table 2.

Table 1
Peak assignments for FTIR spectra data.

	Wavenumber	FTIR peak assignments	Association
(i)	1036	C−C skeletal stretching	Proteins
(ii)	1072	PO$_2$ symmetric stretching	DNA/RNA
(iii)	1152	C−C and C−O stretching	Proteins
(iv)	1220–1280	PO$_2$ asymmetric stretching Amide III	DNA/RNA
(v)	1312	CH$_2$ stretching	Phospholipids
(vi)	1400	CH$_3$ symmetric stretching	Proteins
(vii)	1456	CH$_3$ asymmetric stretching	Proteins
(viii)	1546	Amide II	Proteins
(ix)	1620–1700	Amide I	Proteins
(x)	1742	Ester, C═O stretching	Lipids
(xi)	2854	CH$_2$ symmetric stretching	Lipids
(xii)	2926	CH$_2$ asymmetric stretching	Lipids

more osteoblast phenotype with a pronounced, large spherical nucleus [Fig. 2a(ii–iii)]. Alizarin red staining confirmed the presence of calcium deposits in St-Osteo when compared to bm-MSC [Fig. 2a(iv–v)], providing evidence for bm-MSC multipotency in vitro. Osteogenic differentiation of bm-MSC to St-Osteo was analysed by FTIR spectroscopy and a spectrally integrated IR map of a representative population of bm-MSC is presented [Fig. 2a(vi)]. There were notable differences in the St-Osteo mean spectra across the high wavenumber (2000-3500 cm^{-1}) and fingerprint (1000–1800 cm^{-1}) regions [Fig. 2b], in particular, a strong feature at ~1037 cm^{-1} that overlapped the nucleic acid phosphate backbone band at ~1070 cm^{-1} that is commonly assigned to carbonate groups in apatite [26]. There were also notable differences at 2964 cm^{-1} (corresponding to CH$_3$ asymmetric stretching of lipids and proteins) where St-Osteo cells had a greater peak intensity. The loading of the discriminating PC1 demonstrated pronounced increases in the feature at 1037 cm^{-1} for St-Osteo and a reduction of the strong Amide I and Amide III features at 1220–1280 cm^{-1} [Fig. 2b]. PCA identified all significant changes across the FTIR spectroscopic datasets and the scatter plots generated clearly discriminated both groups from each

Table 2
Peak assignments for Raman spectra data.

	Wavenumber	Chemical bond	Association
(i)	785–788	Stretching of DNA related bonds, and DNA/RNA breathing modes	Nucleic acid
(ii)	1004	Phenylalanine	Protein
(iii)	1090	Stretching of DNA related bonds	Nucleic acid
		Stretching of C−N backbone	Protein
(iv)	1127	Stretching of C−N backbone	Protein
		Stretching of C−C	Lipid
(v)	1262	DNA/RNA breathing modes	Nucleic acid
		Amide III	Lipid
(vi)	1319	CH$_2$, CH$_3$ twisting	Lipid
		DNA/RNA breathing modes	Nucleic acid
		CH deformation vibration	Protein
(vii)	1341	DNA/RNA breathing modes	Nucleic acid
		CH deformation vibration	Protein
(viii)	1451	CH$_2$ deformation vibration	Protein/lipid
(ix)	1585	DNA/RNA breathing modes	Nucleic acid
(x)	1619	Tyrosine; tryptophan	Protein
(xi)	1662	DNA/RNA breathing modes	Nucleic acid
		Amide I	Protein
		Fatty acids	Lipid

other [Fig. 2c].

Raman spectra of individual cell nuclei from bm-MSC and St-Osteo were also recorded and the mean spectra are superimposed to reveal clear differences [Fig. 2d]. The most pronounced was the peak at 960 cm^{-1}, clearly indicating the presence of phosphates associated with mineralisation within the St-Osteo cells [Fig. 2d] [27]. Prominent bands at 1030 cm^{-1} and 1070 cm^{-1} associated with phosphate and carbonate groups respectively, were also evident although they were very much weaker compared to the prominent 960 cm^{-1} feature. Several other peaks were observed that clearly separated bm-MSC from their osteogenic progeny and relate to nucleic acid (DNA/RNA) at 788 cm^{-1}, 1338 cm^{-1}, 1490 cm^{-1}, and 1585 cm^{-1} as well as lipids at 1379 cm^{-1} [Fig. 2d]. PCA identified significant changes across the spectrum and the scatter plots generated clearly discriminated both groups from each other [Fig. 2e].

3.2. FTIR and Raman spectroscopy discriminates bone-marrow derived mesenchymal stem cells from their myogenic progeny in vitro

Myogenic differentiation following treatment of bm-MSC with TGF-β1 was confirmed by determining the enrichment of a synonymous SMC epigenetic histone signature at the myosin heavy chain 11 (Myh11) promoter, Myh11 promoter transactivation, SMC differentiation marker transcript levels (Myh11, CNN1) and immunocytochemical detection of the number of Myh11 and CNN1 cells, respectively [Fig. 3]. Chromatin immunoprecipitation (ChIP) analysis of freshly isolated rat aortic SMCs confirmed the enrichment of the specific SMC epigenetic mark, di-methylation of lysine 4 on histone H3 (H3K4me2) at the Myh11 locus [28] concomitant with a lack of enrichment of the tri-methylation of lysine 27 on histone H3 (H3K27me3) mark which is consistent with a general repression of developmental genes [29] [Fig. 3a]. In contrast, bm-MSC were enriched for the H3K27me3 mark at the same locus [Fig. 3a]. Treatment of bm-MSC with TGF-β1 (2 ng/ml) for 7 d increased the level of enrichment of the H3K4me2 mark with a reciprocal diminution of the H3K27me3 mark to levels that were comparable to H3K4me2 and H3K27me3 levels in sub-cultured de-differentiated rat SMCs (ddSMCs) [Fig. 3a]. TGF-β1 treatment also significantly induced Myh11-promoter transactivation [Fig. 3b] after 2 d concomitant with enhanced Myh11 mRNA levels [Fig. 3c]. Furthermore, treatment of bm-MSCs with TGF-β1 (2 ng/ml) for 14 d resulted in a marked increase in the number of Myh11$^+$ and calponin-1 (CNN1$^+$) positive cells, when compared to vehicle control [Fig. 3d]. Similarly, treatment of bm-MSC with Jag-1-Fc resulted in a significant increase in Myh11 and CNN1 mRNA levels after

48 h [Fig. 3e] concomitant with a dramatic increase in the number of smooth muscle cell α-actin (SMA$^+$) and CNN1$^+$ positive cells after 7 d [Fig. 3f].

FTIR maps and mean spectra were recorded for bm-MSC and their myogenic progeny [Fig. 3g]. In both cases, there were significant peak intensity differences in myogenic progeny in the high wavenumber region, > 2500 cm^{-1}, in particular, between 2800 cm^{-1} and 3000 cm^{-1} [Fig. 3 g] which is associated with acyl chain stretching vibrations from fatty acids of lipids [30]. There were also significant spectral differences in bands in the C−H stretching region associated with absorbance from lipids (3050-2800 cm^{-1}), the amide I and II region associated with protein absorbance (1700–1500 cm^{-1}), and in the lower wavenumber region associated with nucleic acids (1300–1000 cm^{-1}) [Fig. 3g]. Notably, PCA of the FTIR spectroscopic data demonstrated that bm-MSCs could be clearly separated from their myogenic progeny according to the first principal component (PC1) [Fig. 3h]. Moreover, 3-way multivariate statistical analysis revealed that bm-MSC could be clearly discriminated from their myogenic progeny, independent of the inductive stimulus to generate the progeny [Fig. 3h].

3.3. FTIR spectroscopic comparisons between de-differentiated SMC, MSCs and stem cell derived myogenic progeny

Morphological analysis of dissociated rat aortic SMC grown in culture up to passage 4 (ddSMCs) exhibited strong cytoplasmic refractivity, an oval nucleus and rich cytoplasm and overlapped when confluent, forming typical SMC 'peak-to-valley' growth, as previously reported [31]. The two major morphological phenotypes were 'spindle shaped' and 'epithelioid' [Fig. 4a]. In contrast, the majority of myogenic progeny [St-SMC-TGF-β1] were spindle-like cells without a strong cytoplasmic refractivity [Fig. 4a]. The levels of SMA and Myh11 protein and Myh11 mRNA transcripts were significantly reduced in ddSMC when compared to freshly isolated rat aortic SMCs and were comparable to the levels present in stem cell-derived myogenic progeny [St-SMC-TGF-β1] [Fig. 4b, c].

FTIR maps and mean spectra were recorded and analysed for ddSMCs and compared to both undifferentiated bm-MSCs and their myogenic (St-SMC-TGF-β1) and osteogenic progeny (St-Osteo), respectively [Fig. 4d], before PCA analysis of the spectroscopic datasets was performed [Fig. 4e]. Prominent peaks were observed for ddSMCs across the high wavenumber (2000-3500 cm^{-1}) and fingerprint (1000-1800 cm^{-1}) regions of the spectrum. In particular, the main spectral characteristics were bands at ~1540 cm^{-1} and 1650 cm^{-1} (amide I and II, respectively), ~1060 cm^{-1}, 1225 cm^{-1} and 1460 cm^{-1} (C−C and C−H bending) and ~2850 cm^{-1}–2960 cm^{-1} and 3325 cm^{-1}. The peak at ~1225 cm^{-1}, associated with phosphate stretching modes, was noticeably reduced in both ddSMC and St-Osteo cells, when compared undifferentiated bm-MSC and their myogenic progeny [Fig. 4d], respectively, as were the peaks at 1380 cm^{-1} and 1660 cm^{-1} (associated with amide I and II proteins) and 2850–2960 cm^{-1} (associated with distinctive vibrations of N−H, C−H and O−H of lipids and proteins) [Fig. 4d]. In contrast, the ddSMC had a more prominent peak at the ~1036 cm^{-1} and ddSMC and St-Osteo cells at ~3296 cm^{-1} that are associated with proteins [Table 1] [Fig. 4d].

Using 4-way multivariate statistical analysis, there was a significant separation of the four populations by FTIR [Fig. 4e, Table 3] as it successfully discriminated ddSMCs, undifferentiated bm-MSCs and their myogenic (St-SMC-TGF-β1) or osteogenic (St-Osteo) progeny. Moreover, using PCA/LDA, FTIR could discriminate between undifferentiated bm-MSCs from both their myogenic and osteogenic progeny (St-Osteo) with significant confidence even when these daughter cells originated from the same undifferentiated bm-MSC stem cell population [Table 3].
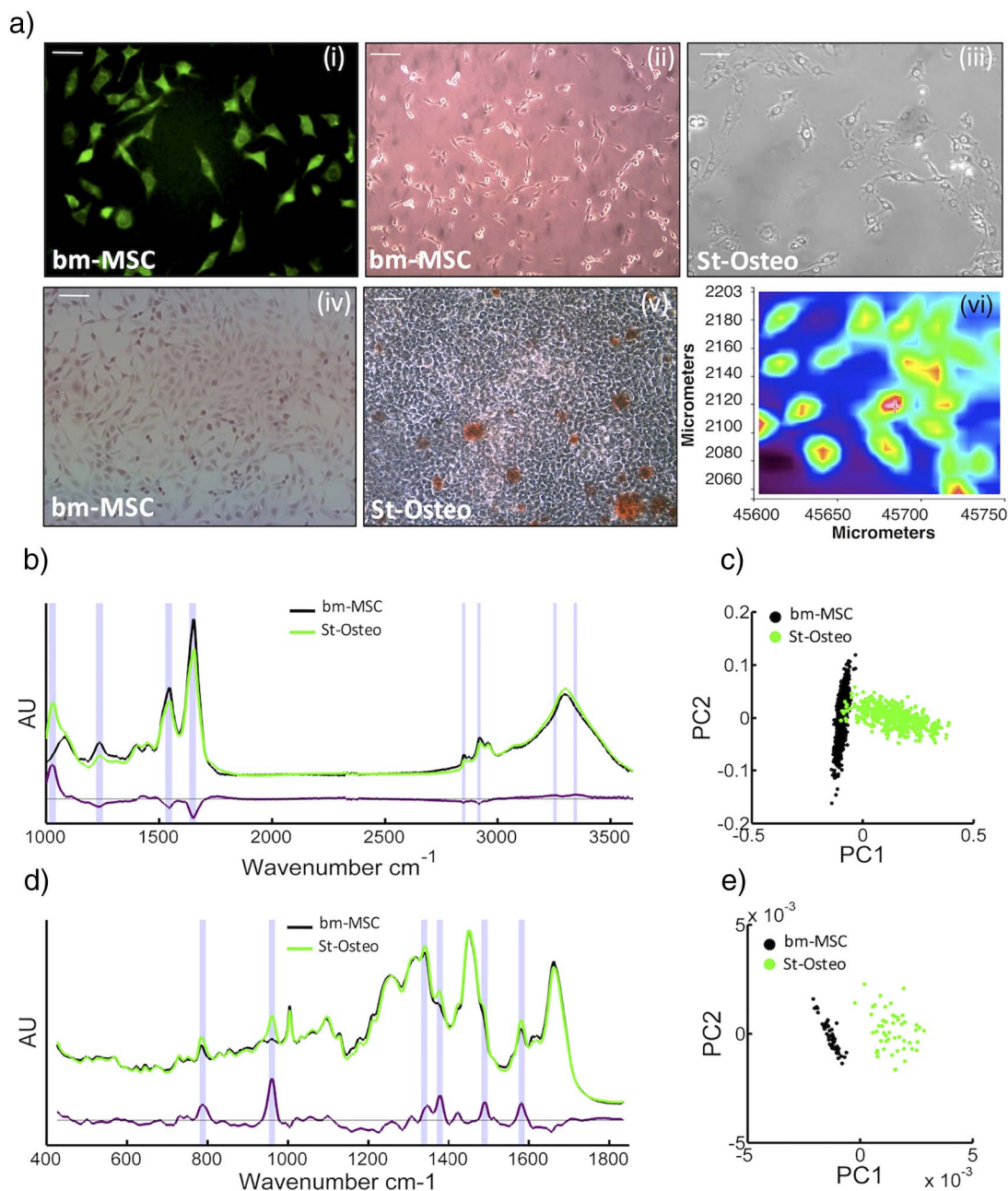
Fig. 2. (a) (i) Representative immunocytochemical image of CD44$^+$ bm-MSC in culture, (ii–iii) phase contrast images and (iv, v) alizarin red staining of bm-MSCs before and after osteogenic differentiation with osteogenic inductive media for 21 d, (vi) representative FTIR heat map of bm-MSCs. (b) Mean FTIR spectra and loading plot of the first principal component and (c) PCA score plot of the bm-MSCs (black) and the St-Osteo (green) cell groups before and after osteogenic differentiation. (d) Mean Raman spectra and loading plot of the first principle component following PCA of the processed bm-MSC and St-Osteo datasets and (e) PCA score plot of bm-MSCs and St-Osteo before and after osteogenic differentiation.

3.4. Raman spectroscopic comparisons between de-differentiated SMC, MSCs and stem cell derived SMC progeny

All four cell populations were separated by multivariate statistical analysis of Raman spectra [Fig. 4f] using a 4-way PCA scatterplot [Fig. 4g, Table 4] with the most notable differences apparent for the St-Osteo spectra [Fig. 4f]. Peak intensities were higher at the 785–788 cm^{-1} and 1585 cm^{-1} correlating to nucleic acids, 960 cm^{-1} corresponding to its strong phosphate peak and the 1375 cm^{-1} associated with proteoglycans [32]. Many other prominent wavenumbers in the loadings for the first two principal components are also highlighted and the wavenumber associations are discussed below [Fig. 4f].

Using PCA/LDA, Raman spectroscopy discriminated undifferentiated bm-MSCs from both their myogenic (St-SMC-TGF-β1) and

osteogenic (St-Osteo) progeny with significant confidence even when these daughter cells originated from the same undifferentiated bm-MSC stem cell population [Table 4].

When the Raman spectra for bm-MSC and their myogenic progeny (St-SMC-TGF-β1) were compared [Fig. 5a], there was a clear separation across both of the first two components [Fig. 5b]. Analysis of the prominent spectral features in both PC1 and PC2 for these cells revealed significant spectral differences relating to nucleic acid (DNA/RNA) at 788 cm^{-1}, 1090 cm^{-1}, 1262 cm^{-1}, 1338 cm^{-1}, 1373 cm^{-1}, 1490 cm^{-1}, and 1581 cm^{-1}; proteins at 1004 cm^{-1}, 1053 cm^{-1} and 1614–1619 cm^{-1}; and lipids at 1262 cm^{-1}, 1300 cm^{-1}, 1379 cm^{-1}, 1439–1454 cm^{-1} and 1650 cm^{-1}–1695 cm^{-1}, respectively [Fig. 5a].

When the Raman spectra for ddSMC were compared to bm-MSC [Fig. 5c], there was a clear separation across only the first component
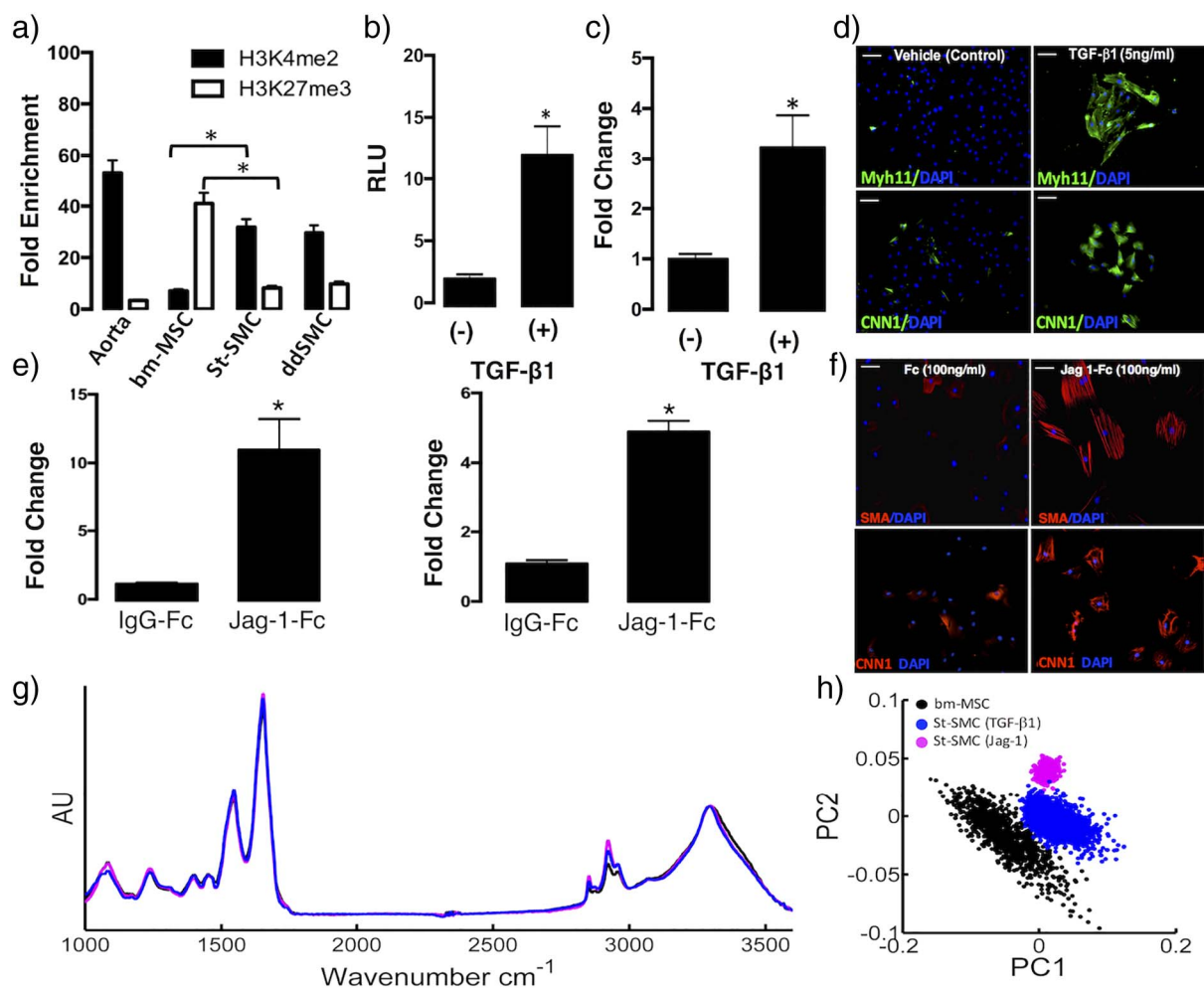
Fig. 3. (a) Representative Chromatin Immunoprecipitation (ChIP) analysis of H3K4me and H4K27me3 enrichment at the Myh11 locus in freshly isolated differentiated aortic SMCs, sub-cultured ddSMCs and bm-MSCs before and after myogenic differentiation with TGF-β1 (2 ng/ml) for 7 d. Data are the mean ± SEM of three samples and are representative of 3 similar experiments (b) Myh11 promoter transactivation and (c) Myh11 mRNA expression levels in bm-MSCs before and after myogenic differentiation with TGF-β1 (2 ng/ml) for 2 d. Data are the mean ± SEM of three experiments (d) representative immunocytochemical analysis of the number of Myh11$^+$ and CNN1$^+$ cells before and after myogenic differentiation of bm-MSC with TGF-β1 (2 ng/ml) for 7 d, (e) CNN1 and Myh11 mRNA levels before and after myogenic differentiation with Jagged1 (2 μg/ml) for 2 d and (f) representative immunocytochemical analysis of the number of SMA$^+$ and CNN1$^+$ before and after myogenic differentiation with Jag-1 (100 ng/ml) for 5 d. (g) Mean FTIR spectra and (h) scatter plot of the first principal component after PCA for bm-MSCs before and after myogenic differentiation with TGF-β1 (2 ng/ml) and Jag-1 (2 μg/ml) for 14 d.

[Fig. 5d], and the loading for only this component is shown [Fig. 5c]. Many of the spectral differences recorded for bm-MSC *versus* St-SMCs (TGF-β1) were also observed when ddSMC were compared bm-MSC [Fig. 5c]. In addition to sharing these peaks, more peaks were observed in PC1 that relate to nucleic acid at 813 cm^{-1} and 1420 cm^{-1}; proteins at 1031 cm^{-1}; and lipids at 1220–1250 cm^{-1}, 1420 cm^{-1} and 1554 cm^{-1}.

In contrast, when the Raman spectra of ddSMC were compared to St-SMC (TGF-β1), there were significant similarities between both spectra with sharp bands at the 1004 cm^{-1}, 1262 cm^{-1}, 1319 cm^{-1}, 1585 cm^{-1} and 1662 cm^{-1} [Fig. 5e]. Some differences were observed at 788 cm^{-1}, 1319 cm^{-1} and 1585 cm^{-1}, corresponding to nucleic acid content, indicative of differences between the DNA/RNA content of the St-SMCs (TGF-β1) and the ddSMCs [Fig. 5e]. Further differences were observed in the region of 1262 cm^{-1} attributable to the nucleic acid guanine and amide III and at 1619 cm^{-1} attributable to tyrosine or tryptophan [Fig. 5e]. Raman spectra of ddSMCs were further compared to St-Osteo and revealed significant differences in the spectra of these two populations, consistent primarily with the onset of mineralization [data not shown]. Finally, PCA analysis of Raman spectra could not directly separate the St-SMCs (TGF-β1) and ddSMC groups with 100% accuracy [Fig. 5f]. However, classification of both cell populations was

achieved using a combination of PCA and LDA when applied to each of the four experimental groups. The ddSMC were classified correctly with 89.7% sensitivity and the St-SMC (TGF-β1) correctly with a 92.7% sensitivity on a leave-one-out cross validation method (Table 4).

4. Discussion

Vibrational spectroscopy has shown great promise in functional analysis of single cells and in label-free detection of diseases [14]. Raman micro-spectroscopy is normally performed in a point to point mapping mode, and thus is considerably slower than FTIR in imaging mode. Nevertheless, its higher spatial and spectral resolution favours it for cellular and subcellular analysis, rather than large scale screening of cell populations [16,33]. Multivariate statistical techniques such as Principal Components Analysis (PCA) and Discriminant Analysis (DA) have significantly contributed to the development of diagnostic algorithms based on the information recovered in Raman and FTIR spectral signatures. However, before vibrational spectroscopy can be fully implemented as a diagnostic platform, cross-validation with known immunohistochemical platforms for biomarker detection is required [34]. In this context, the current study has established for the first time that vibrational spectroscopy can discriminate undifferentiated stem cells
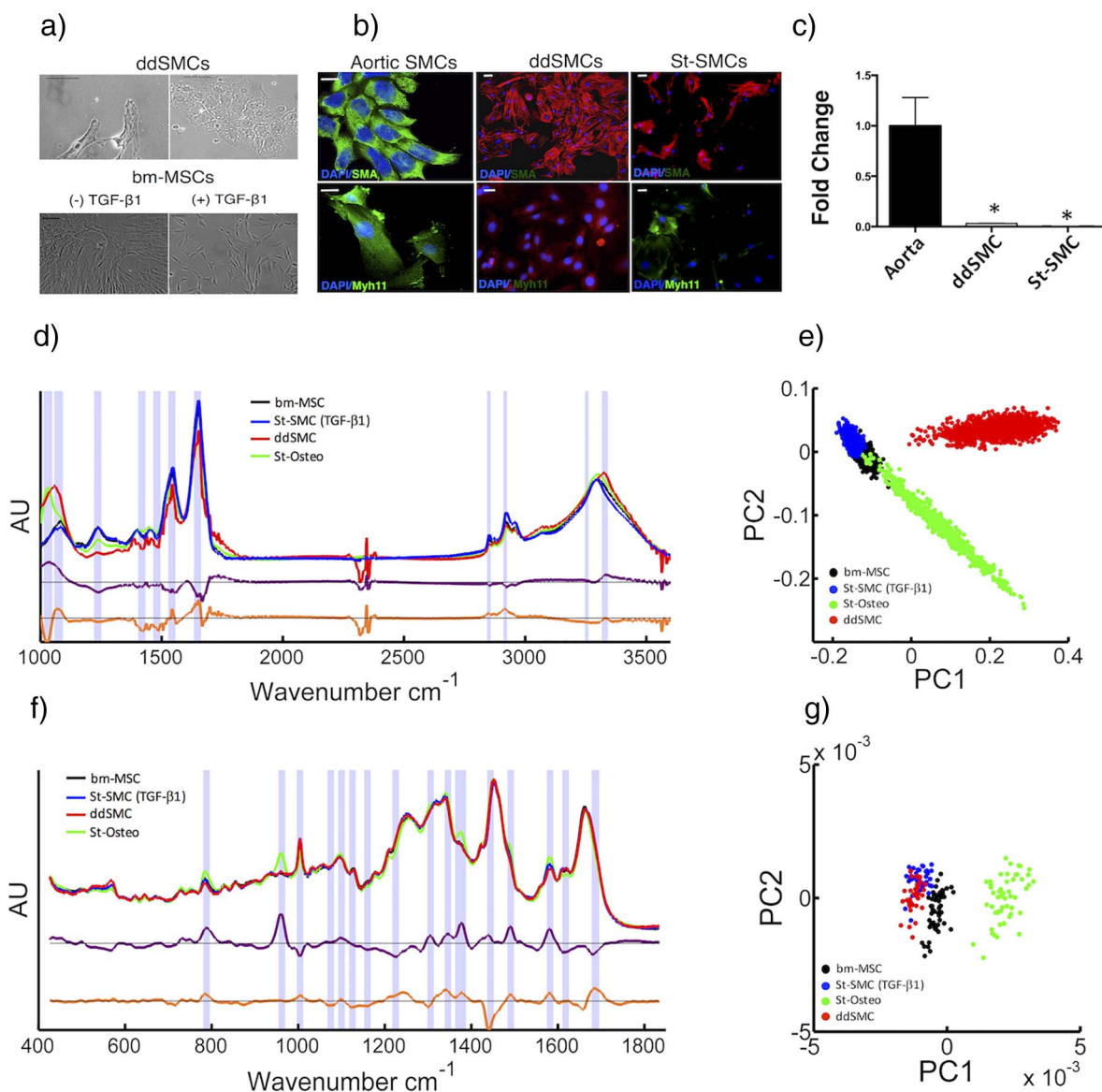
Fig. 4. (a) Representative phase contrast images of freshly isolated aortic SMCs and St-SMCs following TGF-β1 induced myogenic differentiation. (b) Immunocytochemical analysis of SMA and Myh11 expression and (c) quantitative qRT-PCR of Myh11 mRNA levels in freshly isolated aortic SMCs, sub-cultured ddSMCs (passage 4) and St-SMCs following TGF-β1 induced myogenic differentiation. (d) Mean FTIR spectra and (e) a 4-way scatter plot of the first two principal components after PCA of bm-MSCs, ddSMCs, St-SMCs (TGF-β1) and St-Osteo. (f) Mean Raman spectra and (g) a 4-way scatter plot of the first two principal components after PCA for bm-MSCs, ddSMCs, St-SMCs (TGF-β1) and St-Osteo.

Table 3
Confusion matrix for PCA-LDA of FTIR spectral data showing the percentage classification for each cell type. Values on the diagonal represent those correctly identified, off-diagonal values represent those incorrectly identified.

	bm-MSC	St-Osteo	ddSMC	St-SMC
bm-MSC	94	0	3	3
St-Osteo	0	100	0	0
ddSMC	7	1	92	0
St-SMC	0	0	0	100

Table 4
Confusion matrix for PCA-LDA of Raman spectral data showing the percentage classification for each cell type. Values on the diagonal represent those correctly identified, off-diagonal values represent those incorrectly identified.

	bm-MSC	St-Osteo	ddSMC	St-SMC
bm-MSC	100	0	0	0
St-Osteo	0	100	0	0
ddSMC	0	0	89.7	10.3
St-SMC	0	0	7.3	92.7

from their myogenic and osteogenic progeny *in vitro* following validation using conventional genetic, biochemical and histological analyses.

While several studies have confirmed the accuracy of Raman spectroscopy in various biological tissues such as the cervical lesions, gastric tissues, colon, thyroid, larynx, skin, bladder amongst others [14], data on the interrogation of vascular tissue for early signs of disease have been limited [35]. The accumulation of neointimal SMC-like cells within the vessel wall leading to the obstruction of blood flow represents a major hallmark of cardiovascular disease [3]. Recent lineage tracing studies in mice and biomarker identification in human vessels have provided compelling evidence that stem cell-derived myogenic progeny (either directly or *via* endothelial-mesenchymal-transition) in addition to de-differentiated SMCs may be responsible for neointimal formation [4,7,9,36]. Hence the ability to discriminate de-differentiated SMC from undifferentiated stem cells and their myogenic and osteogenic progeny within the vessel wall and map their respective
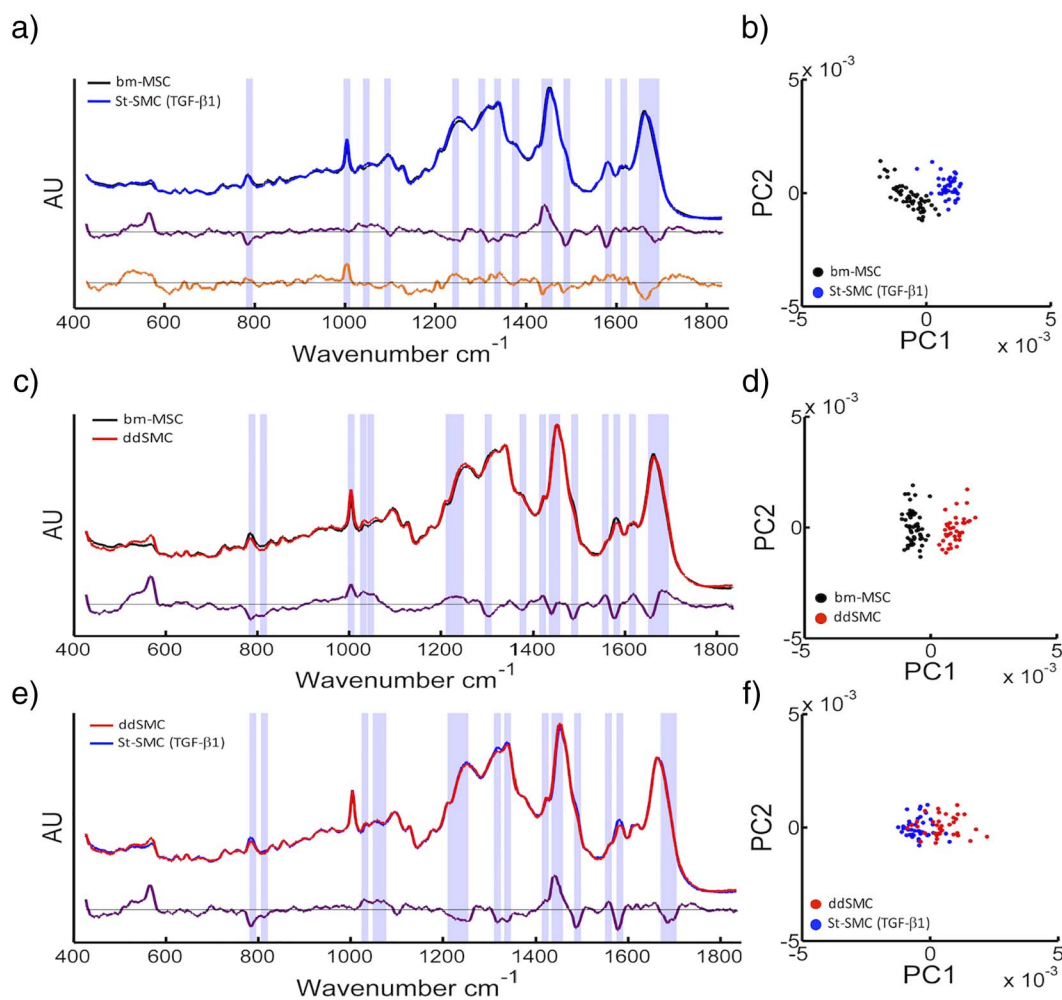
Fig. 5. (a) Mean Raman spectra and the loadings corresponding to the first two principal components for bm-MSC and the St-SMCs-TGF-β1 following myogenic differentiation. Significant peaks in the loadings of PC1 and PC2 are highlighted and (b) corresponding scatter plot for the first two principle components for bm-MSC and the St-SMCs-TGF-β1. Mean Raman spectra and the loadings of the first principle component and corresponding scatter plots for (c, d) bm-MSC *versus* ddSMCs and (e, f) ddSMCs *versus* St-SMC. For (c) and (d), only the first loadings are shown, corresponding only to PC1, since separation is found in this component alone.

accumulation over time using label-free platforms represents an attractive diagnostic platform for vascular proliferative disease.

Our studies reveal for the first time that FTIR detects specific alterations in the cellular profile of nucleic acid, protein and lipid content of bm-MSC when they progress towards a distinct myogenic phenotype *in vitro*. Moreover, Raman further distinguished a discriminant alteration in the nuclear spectra for nucleic acid, protein and lipid profiles of these cells. These data highlight the significant screening potential of FTIR and the more analytical potential of Raman at discriminating undifferentiated stem cells from de-differentiated SMCs and stem cell-derived osteogenic and myogenic progeny. Notably, the feasibility of using prototype devices including a laser-scanning fibre endoscope (SFE) to interrogate vascular structure in real-time *in vivo* and detect the early signs of disease has been validated [35,37].

The potential of FTIR to screen cell populations and discriminate undifferentiated stem cells from their osteogenic progeny was first established. In particular, analysis of the FTIR spectra clearly indicated the onset of mineralization *via* the emergence of the feature at 1037 cm^{-1} which is associated with carbonate groups in apatite [38,39]. Interrogation of individual cell nuclei by Raman spectroscopy further distinguished a discriminant alteration in phosphate content *in situ* due to the pronounced peak at 960 cm^{-1} [27] that facilitated identification of these cells from each other by PCA.

TGF-β1 is known to activate a heteromeric complex of two serine/threonine kinase receptors [the type IITGF-β receptor (TβRII) and the

type I receptor, ALK5], that results in phosphorylation-dependent activation of Smads 2 and 3 that subsequently complex with Smad4 and translocate to the nucleus where they stimulate myogenic gene expression [40]. Similarly, Jag-1 binds to specific Notch receptors on the plasma membrane that, once cleaved, act as transcriptional activators of myogenic differentiation [41], including activation of the SMA promoter [42]. Both of these stimuli promoted myogenic differentiation of bm-MSCs *in vitro* by inducing specific epigenetic changes at the Myh11 promoter leading to Myh11 promoter transactivation, increased expression of transcript for SMC differentiation markers (Myh11 and CNN1) concomitant with a significant increase in the number of Myh11^{+}, SMA^{+} and CNN1^{+} positive cells. Interrogation of de-differentiated SMCs (ddSMCs), undifferentiated bm-MSC and their myogenic (St-SMCs) and osteogenic progeny (St-Osteo) by FTIR revealed significant differences in their respective spectral signatures. Notably, the spectra associated with cellular phospholipid content of myogenic progeny decreased when compared to undifferentiated bm-MSC whereas there was a marked increase in levels of −CH$_2$ symmetric and −CH and −CH$_3$ asymmetric stretching associated with proteins and lipids. This was in contrast to osteogenic differentiation where there was a notable marked decrease in levels of −CH$_2$ symmetric and −CH and −CH$_3$ asymmetric stretching. Furthermore, the similarity in the pattern of FTIR spectral changes for both TGF-β1 and Jag-1 myogenic progeny when compared to undifferentiated bm-MSC suggests that these differences are independent of the inductive stimulus and were specifically

associated with a myogenic inductive stimulus and response. Several previous studies have shown a general decrease in nucleic acids in undifferentiated cells compared to their progeny [43] while similar changes in protein composition (*e.g.*, α-helix structures) in stem cells when compared to differentiated cells have been described [43,44]. More recently, FTIR spectra have been used to successfully discriminate functional hepatocyte and chondrocyte progeny from undifferentiated stems cells [rat bone marrow [45] murine ESCs [46] (both hepatocytes), and hMSCs [47](chondrocytes)] based on similar kinds of spectral differences. As stem cell-derived myogenic progeny and de-differentiated SMC were also separated by PCA analysis of their corresponding FTIR spectra, these data collectively suggest that FTIR is a reliable platform to screen and map undifferentiated stem cell populations from their myogenic progeny. Indeed, because of the limit of resolution, the longer wavelength of mid infrared radiation, coupled with the use of multidetector arrays in the Fourier Transform mode, render IR techniques very suitable for mapping larger cell populations or tissue sections [16].

Raman spectroscopy of individual cell nuclei from undifferentiated bm-MSC, their myogenic progeny (St-SMC-TGF-β1) and ddSMCs further defined discrete spectral shifts in these cell populations and quantitatively provided reliable estimates of *in situ* protein, nucleic acids and lipid content of bm-MSCs before and after myogenic and osteogenic differentiation. Nine distinct wavenumber bands within the fingerprint region 600–1800 cm^{-1} were recorded that correspond to broad biochemical groupings [23,30,48]. Analysis of the spectra revealed significant differences that facilitated further discrimination of these cell populations by PCA. Notably, when compared to ddSMC, undifferentiated bm-MSC had higher peaks at 785–788 cm^{-1} and 1585 cm^{-1} which are attributable to nucleic acid content. Similar spectral differences were also observed at 785–788 cm^{-1} for St-SMC. This is not surprising, as stem cells are known to have a higher nucleic acid content than differentiated cells [49,50]. The peak at 1262 cm^{-1} that corresponds to nucleic acid and lipid content has also been associated with collagen [51] and is understandably higher in the ddSMC when compared to bm-MSC. Other notable differences for St-SMC appear at 1319 cm^{-1} and 1341 cm-1 and are associated with lipids, nucleic acids and proteins in addition to a higher peak at 1585 cm^{-1} which corresponds to nucleic acids.

Importantly, there was a clear separation observed across the first principle component for bm-MSCs and St-SMCs and for bm-MSC and ddSMCs by FTIR suggesting that these cell populations are clearly distinct. However, interrogation by Raman across the first principle component failed to separate these populations with 100% accuracy. This is not unexpected since FTIR datasets are from whole cell spectra while Raman spectra were generated exclusively from the cell nucleus. The spectral differences within the cytoplasm may be more pronounced as these cells begin to fate towards a myogenic lineage but still retain significant differences within their cytoplasmic content. It is also clear that significant epigenetic and genetic changes occur early within the nucleus of bm-MSC as they undergo myogenic differentiation [28] and these specific changes shared the greatest similarity with the ddSMCs. Furthermore, since ddSMCs may be primarily derived from resident stem cells as they grow and expand at an increased rate in culture [4], it is not surprising that the Raman spectral profile for myogenic progeny shared the greatest similarity with de-differentiated SMC cells. Although PCA analysis did not separate the St-SMCs (TGF-β1) and ddSMC groups with 100% accuracy, classification of both cell lines was eventually achieved using a combination of PCA and LDA suggesting that there are also important differences, despite these similarities.

A primary limitation of the current study is that the bm-MSC population were of rodent origin, heterogeneous in nature and expanded in culture media that is different from protocols required for pre-clinical and clinical studies. Moreover, spectral measurements were taken with cell cultures, rather than being obtained from an intact vessel *in situ*. Culturing the progeny of a single CFU or phenotype-isolated single clonogenic human stem cell would give rise to a more homogenous "true" human MSC population that could serve to provide similar results and further validate vibrational spectroscopic for clinical applications. Vibrational spectroscopy for *ex vivo* analysis of various tissues affected by vascular diseases, including atherosclerotic plaque, vessel wall remodelling and endothelial dysfunction has been performed [52] [51]. The Raman spectral differences in remodelled vessels following IMT originated mainly from the protein features within the main bands at 1660 cm^{-1} (amide I), 1244 cm^{-1} (amide III), and at 1004 cm^{-1} (phenylalanine). In the spectrum of normal intimal SMCs, major bands due to amide I (1656 cm^{-1}), amide II (1556 cm^{-1}), and CH bending (1457 cm^{-1}) vibrations of the proteins collagen and elastin have also been reported [35,52,53]. In the spectrum of the intima of non-calcified atherosclerotic plaque, major bands due to both proteins and lipids are also observed. The lipid bands at 1734 cm^{-1}, 1468 cm^{-1}, 1171 cm^{-1} and 1058 cm^{-1} were assigned to the C = O (ester) stretch, CH_2 bend, C—O (ester) stretch and C—O stretch, respectively [35]. Our current study suggests that St-SMCs exhibit similar enhanced spectral intensities at peaks at 1004 cm^{-1} 1451 cm^{-1} and 1662 cm^{-1} when compared to bm-MSCs and ddSMCs respectively, suggesting that these peak intensities might represent a specific photonic signature for stem cell myogenic progeny that could be exploited diagnostically. Furthermore, as vascular lesions are often calcified [3], the ability to discriminate between St-Osteo and St-SMCs is also an advantage. Our data suggests that both FTIR and Raman can detect differences between myogenic and osteogenic progeny even when they are derived from the same undifferentiated stem cell.

In conclusion, vibrational spectroscopy was successfully applied to the study of bm-MSCs before and after myogenic differentiation *in vitro* to identify discrete spectral characteristics that could facilitate localisation and detection of myogenic differentiation of resident vascular stem cell populations *in vivo*. The vasculature is unique in that it has a well-defined spatial morphology of cells either side and within the internal (IEL) and external elastic lamina (EEL) that could facilitate acquisition of label-free analysis of cell spectra with relative confidence. The initial step in the development of arteriosclerotic disease is IMT and neointimal formation that facilitates the build-up of LDL (low density lipoprotein) particles within the intimal layer of the vessel wall [54,55]. Interrogation of early atherosclerotic vessels *in situ* using vibrational spectroscopy could discriminate the presence of stem cell-derived progeny not readily available in current diagnostic imaging techniques such as IVUS, MRI, and angiography. Indeed, significant progress has already been made towards *in vivo* application of vibrational spectroscopy. Raman spectroscopy in particular, as an optical probe, lends itself naturally to endoscopic application and has recently been deployed for intra-operative guidance of brain surgery [56] and endoscopic gastrointestinal procedures [57]. A smart Raman needle probe has also been developed and tested for potential *in vivo* and *ex vivo* use, capable of measuring Raman molecular tissue signals in < 1–2 s down a hypodermic needle [58]. Because of its high sensitivity to water, there have been relatively fewer *in vivo* applications of IR spectroscopy, although the recent emergence of high brightness, tunable Quantum Cascade Lasers has opened the door towards their development [59]. This suggests that, with further development, FTIR could provide initial selection of cells for interrogation before quantitative chemical and morphological evaluation by Raman discriminates these cells within vascular lesions *in situ*, such as the presence of stem cell derived myogenic or osteogenic progeny so that more targeted therapies against these discrete phenotypes can be introduced. Finally, circulating vascular cells and progenitor cells shed from the vessel wall during IMT and disease progression could be retrieved from blood and interrogated for clinical evaluation using vibrational spectroscopy to provide a more definitive tool for early diagnosis [60]. The ability to assess the accumulation of stem cell-derived progeny using label free platforms *in situ* or the shedding of these progeny into the blood during disease progression may further facilitate interrogation of these phenotypes by

their discrete spectroscopic signatures using liquid biopsies and microfluidic platforms.

Transparency document

The Transparency document associated with this article can be found, in online version.

Author contributions

CM, JM, AM, BH and HJB performed the label-free spectroscopic experiments; CM, RH, DB, GC and MDL performed all the cell biology experiments; BH, HJP and PAC supervised and analysed the results and created the figures; BH, HJB and PAC designed the research and wrote the paper. All authors read and approved the manuscript.

Acknowledgements

Appendix A. Supplementary data

Supplementary data to this article can be found online at https://doi.org/10.1016/j.bbamcr.2017.11.006.

References

[1] V.H. Tank, R. Ghosh, V. Gupta, N. Sheth, S. Gordon, W. He, et al., Drug eluting stents versus bare metal stents for the treatment of extracranial vertebral artery disease: a meta-analysis, J. Neurointerv. Surg. 8 (2016) 770–774, http://dx.doi.org/10.1136/neurintsurg-2015-011697.

[2] F. Alfonso, R.A. Byrne, F. Rivero, A. Kastrati, Current treatment of in-stent restenosis, J. Am. Coll. Cardiol. 63 (2014) 2659–2673, http://dx.doi.org/10.1016/j.jacc.2014.02.545.

[3] M.R. Bennett, S. Sinha, G.K. Owens, Vascular smooth muscle cells in atherosclerosis, Circ. Res. 118 (2016) 692–702, http://dx.doi.org/10.1161/CIRCRESAHA.115.306361.

[4] F. Yuan, D. Wang, K. Xu, J. Wang, Z. Zhang, L. Yang, et al., Contribution of vascular cells to neointimal formation, PLoS One 12 (2017) e0168914, , http://dx.doi.org/10.1371/journal.pone.0168914.

[5] Z. Tang, A. Wang, F. Yuan, Z. Yan, B. Liu, J.S. Chu, et al., Differentiation of multipotent vascular stem cells contributes to vascular diseases, Nat. Commun. 3 (2012) 875, http://dx.doi.org/10.1038/ncomms1867.

[6] M. Wan, C. Li, G. Zhen, K. Jiao, W. He, X. Jia, et al., Injury-activated transforming growth factor β controls mobilization of mesenchymal stem cells for tissue remodeling, Stem Cells 30 (2012) 2498–2511, http://dx.doi.org/10.1002/stem.1208.

[7] R. Kramann, C. Goettsch, J. Wongboonsin, H. Iwata, R.K. Schneider, C. Kuppe, et al., Adventitial MSC-like cells are progenitors of vascular smooth muscle cells and drive vascular calcification in chronic kidney disease, Cell Stem Cell 19 (2016) 628–642, http://dx.doi.org/10.1016/j.stem.2016.08.001.

[8] B.C. Cooley, J. Nevado, J. Mellad, D. Yang, C. St Hilaire, A. Negro, et al., TGF-β signaling mediates endothelial-to-mesenchymal transition (EndMT) during vein graft remodeling, Sci. Transl. Med. 6 (2014), http://dx.doi.org/10.1126/scitranslmed.3006927 (227ra34–227ra34).

[9] J. Chappell, J.L. Harman, V.M. Narasimhan, H. Yu, K. Foote, B.D. Simons, et al., Extensive proliferation of a subset of differentiated, yet plastic, medial vascular smooth muscle cells contributes to neointimal formation in mouse injury and atherosclerosis models, Circ. Res. 119 (2016) 1313–1323, http://dx.doi.org/10.1161/CIRCRESAHA.116.309799.

[10] S. Chen, R.J. Lechleider, Transforming growth factor-beta-induced differentiation of smooth muscle from a neural crest stem cell line, Circ. Res. 94 (2004) 1195–1202, http://dx.doi.org/10.1161/01.RES.0000126897.41658.81.

[11] K. Kurpinski, H. Lam, J. Chu, A. Wang, A. Kim, E. Tsay, et al., Transforming growth factor-beta and notch signaling mediate stem cell differentiation into smooth muscle cells, Stem Cells 28 (2010) 734–742, http://dx.doi.org/10.1002/stem.319.

[12] L. Pang, C. Wei, J. Duan, H. Zou, W. Cao, Y. Qi, et al., TGF-β1/Smad signaling, MMP-14, and MSC markers in arterial injury: discovery of the molecular basis of restenosis, Int. J. Clin. Exp. Pathol. 7 (2014) 2915–2924.

[13] E.M. Redmond, W. Liu, K. Hamm, E. Hatch, P.A. Cahill, D. Morrow, Perivascular delivery of Notch 1 siRNA inhibits injury-induced arterial remodeling, PLoS One 9 (2014) e84122, , http://dx.doi.org/10.1371/journal.pone.0084122.

[14] J.-X. Cheng, X.S. Xie, Vibrational spectroscopic imaging of living systems: an emerging platform for biology and medicine, Science 350 (2015), http://dx.doi.org/10.1126/science.aaa8870 (aaa8870–aaa8870).

[15] J.N. Miller, Applied infrared infrared spectroscopy: fundamentals, techniques and analytical problem-solving, Anal. Chim. Acta 138 (1982) 433–434, http://dx.doi.org/10.1016/S0003-2670(01)85346-0.

[16] H.J. Byrne, P. Knief, M.E. Keating, F. Bonnier, Spectral pre and post processing for infrared and Raman spectroscopy of biological tissues and cells, Chem. Soc. Rev. 45 (2016) 1865–1878, http://dx.doi.org/10.1039/c5cs00440c.

[17] E. Efeoglu, A. Casey, H.J. Byrne, In vitro monitoring of time and dose dependent cytotoxicity of aminated nanoparticles using Raman spectroscopy, Analyst 141 (2016) 5417–5431, http://dx.doi.org/10.1039/C6AN01199C.

[18] S.M. Ali, F. Bonnier, H. Lambkin, K. Flynn, V. McDonagh, C. Healy, et al., A comparison of Raman, FTIR and ATR-FTIR micro spectroscopy for imaging human skin tissue sections, Anal. Methods 5 (2013) 2281–2291, http://dx.doi.org/10.1039/c3ay40185e.

[19] P.A. Cahill, A. Hassid, Differential antimitogenic effectiveness of atrial natriuretic peptides in primary versus subcultured rat aortic smooth muscle cells: relationship to expression of ANF-C receptors, J. Cell. Physiol. 154 (1993) 28–38, http://dx.doi.org/10.1002/jcp.1041540105.

[20] E. Kennedy, C.J. Mooney, R. Hakimjavadi, E. Fitzpatrick, S. Guha, L.E. Collins, et al., Adult vascular smooth muscle cells in culture express vascular stem cell markers typical of resident multipotent vascular stem cells, Cell Tissue Res. 358 (2014) 203–216, http://dx.doi.org/10.1007/s00441-014-1937-2.

[21] E. Kennedy, R. Hakimjavadi, C. Greene, C.J. Mooney, E. Fitzpatrick, L.E. Collins, et al., Embryonic rat vascular smooth muscle cells revisited - a model for neonatal, neointimal SMC or differentiated vascular stem cells? Vasc. Cell. 6 (2014) 6, http://dx.doi.org/10.1186/2045-824X-6-6.

[22] L.T. Kerr, T.M. Lynn, I.M. Cullen, P.J. Daly, N. Shah, S. O'Dea, et al., Methodologies for bladder cancer detection with Raman based urine cytology, Anal. Methods 8 (2016) 4991–5000, http://dx.doi.org/10.1039/c5ay03000d.

[23] L.T. Kerr, B.M. Hennelly, A multivariate statistical investigation of background subtraction algorithms for Raman spectra of cytology samples recorded on glass slides, Chemom. Intell. Lab. Syst. 158 (2016) 61–68, http://dx.doi.org/10.1016/j.chemolab.2016.08.012.

[24] P. Bassan, H.J. Byrne, J. Lee, F. Bonnier, C. Clarke, P. Dumas, et al., Reflection contributions to the dispersion artefact in FTIR spectra of single biological cells, Analyst 134 (2009) 1171, http://dx.doi.org/10.1039/b821349f.

[25] C. Hughes, M. Liew, A. Sachdeva, P. Bassan, P. Dumas, C.A. Hart, et al., SR-FTIR spectroscopy of renal epithelial carcinoma side population cells displaying stem cell-like characteristics, Analyst 135 (2010) 3133, http://dx.doi.org/10.1039/c0an00574f.

[26] A. Awonusi, M.D. Morris, M.M.J. Tecklenburg, Carbonate assignment and calibration in the Raman spectrum of apatite, Calcif. Tissue Int. 81 (2007) 46–52, http://dx.doi.org/10.1007/s00223-007-9034-0.

[27] L.L. McManus, F. Bonnier, G.A. Burke, B.J. Meenan, A.R. Boyd, H.J. Byrne, Assessment of an osteoblast-like cell line as a model for human primary osteoblasts using Raman spectroscopy, Analyst 137 (2012) 1559–1569, http://dx.doi.org/10.1039/c2an16209a.

[28] D. Gomez, P. Swiatlowska, G.K. Owens, Epigenetic control of smooth muscle cell identity and lineage memory, Arterioscler. Thromb. Vasc. Biol. 35 (2015) 2508–2516, http://dx.doi.org/10.1161/ATVBAHA.115.305044.

[29] J. Van der Meulen, F. Speleman, P. Van Vlierberghe, The H3K27me3 demethylase UTX in normal development and disease, Epigenetics 9 (2014) 658–668, http://dx.doi.org/10.4161/epi.28298.

[30] Z. Movasaghi, S. Rehman, I.U. Rehman, Raman spectroscopy of biological tissues, Appl. Spectrosc. Rev. 42 (2007) 493–541, http://dx.doi.org/10.1080/05704920701551530.

[31] H. Hao, G. Gabbiani, M.-L. Bochaton-Piallat, Arterial smooth muscle cell heterogeneity: implications for atherosclerosis and restenosis development, Arterioscler. Thromb. Vasc. Biol. 23 (2003) 1510–1520, http://dx.doi.org/10.1161/01.ATV.0000090130.85752.ED.

[32] S. Gamsjaeger, R. Mendelsohn, A.L. Boskey, S. Gourion-Arsiquaud, K. Klaushofer, E.P. Paschalis, Vibrational spectroscopic imaging for the evaluation of matrix and mineral chemistry, Curr. Osteoporos. Rep. 12 (2014) 454–464, http://dx.doi.org/10.1007/s11914-014-0238-8.

[33] H.J. Byrne, G.D. Sockalingum, N. Stone, Raman microscopy: complement or competitor? Biomedical Applications of Synchrotron Infrared Microspectroscopy, Royal Society of Chemistry, Cambridge, 2010, pp. 105–143, , http://dx.doi.org/10.1039/9781849731997-00105 (Chapter 4).

[34] J. Sulé-Suso, N.R. Forsyth, V. Untereiner, G.D. Sockalingum, Vibrational spectroscopy in stem cell characterisation: is there a niche? Trends Biotechnol. 32 (2014) 254–262, http://dx.doi.org/10.1016/j.tibtech.2014.03.002.

[35] J.T. Motz, M. Fitzmaurice, A. Miller, S.J. Gandhi, A.S. Haka, L.H. Galindo, et al., In vivo Raman spectral pathology of human atherosclerosis and vulnerable plaque, J. Biomed. Opt. 11 (2006) 021003, , http://dx.doi.org/10.1117/1.2190967.

[36] E. Torsney, K. Mandal, A. Halliday, M. Jahangiri, Q. Xu, Characterisation of progenitor cells in human atherosclerotic vessels, Atherosclerosis 191 (2007) 259–264, http://dx.doi.org/10.1016/j.atherosclerosis.2006.05.033.

[37] L.E. Savastano, Q. Zhou, A. Smith, K. Vega, C. Murga-Zamalloa, D. Gordon, et al., Multimodal laser-based angioscopy for structural, chemical and biological imaging of atherosclerosis, Nat. Biomed. Eng. 1 (2017) 0023, http://dx.doi.org/10.1038/s41551-016-0023.

[38] J.A. Leopold, Vascular calcification: mechanisms of vascular smooth muscle cell calcification, Trends Cardiovasc. Med. 25 (2015) 267–274, http://dx.doi.org/10.1016/j.tcm.2014.10.021.

[39] L. Louvet, D. Bazin, J. Büchel, S. Steppan, J. Passlick-Deetjen, Z.A. Massy,

Characterisation of calcium phosphate crystals on calcified human aortic vascular smooth muscle cells and potential role of magnesium, PLoS One 10 (2015) e0115342, , http://dx.doi.org/10.1371/journal.pone.0115342.

[40] J. Massague, Smad transcription factors, Genes Dev. 19 (2005) 2783–2810, http://dx.doi.org/10.1101/gad.1350705.

[41] D. Morrow, S. Guha, C. Sweeney, Y. Birney, T. Walshe, C. O'Brien, et al., Notch and vascular smooth muscle cell phenotype, Circ. Res. 103 (2008) 1370–1382, http://dx.doi.org/10.1161/CIRCRESAHA.108.187534.

[42] M. Noseda, Y. Fu, K. Niessen, F. Wong, L. Chang, G. McLean, et al., Smooth muscle alpha-actin is a direct target of Notch/CSL, Circ. Res. 98 (2006) 1468–1470, http://dx.doi.org/10.1161/01.RES.0000229683.81357.26.

[43] D. Ami, T. Neri, A. Natalello, P. Mereghetti, S.M. Doglia, M. Zanoni, et al., Embryonic stem cell differentiation studied by FT-IR microspectroscopy, Biochim. Biophys. Acta Mol. Cell Res. 1783 (2008) 98–106, http://dx.doi.org/10.1016/j.bbamcr.2007.08.003.

[44] P. Heraud, E.S. Ng, S. Caine, Q.C. Yu, C. Hirst, R. Mayberry, et al., Fourier transform infrared microspectroscopy identifies early lineage commitment in differentiating human embryonic stem cells, Stem Cell Res. 4 (2010) 140–147, http://dx.doi.org/10.1016/j.scr.2009.11.002.

[45] D. Ye, W. Tanthanuch, K. Thumanu, A. Sangmalee, R. Parnpai, P. Heraud, Discrimination of functional hepatocytes derived from mesenchymal stem cells using FTIR microspectroscopy, Analyst 137 (2012) 4774–4784, http://dx.doi.org/10.1039/c2an35329f.

[46] K. Thumanu, W. Tanthanuch, D. Ye, A. Sangmalee, C. Lorthongpanich, R. Parnpai, et al., Spectroscopic signature of mouse embryonic stem cell-derived hepatocytes using synchrotron Fourier transform infrared microspectroscopy, J. Biomed. Opt. 16 (2011) 057005, , http://dx.doi.org/10.1117/1.3580253.

[47] C. Chonanant, N. Jearanaikoon, C. Leelayuwat, T. Limpaiboon, M.J. Tobin, P. Jearanaikoon, et al., Characterisation of chondrogenic differentiation of human mesenchymal stem cells using synchrotron FTIR microspectroscopy, Analyst 136 (2011) 2542–2551, http://dx.doi.org/10.1039/c1an15182g.

[48] I.R.M. Ramos, A. Malkin, F.M. Lyng, Current advances in the application of Raman spectroscopy for molecular diagnosis of cervical cancer, Biomed. Res. Int. 2015 (2015) 561242–561249, http://dx.doi.org/10.1155/2015/561242.

[49] J.W. Chan, D.K. Lieu, Label-free biochemical characterization of stem cells using vibrational spectroscopy, J. Biophotonics 2 (2009) 656–668, http://dx.doi.org/10.1002/jbio.200910041.

[50] I. Notingher, I. Bisson, J.M. Polak, L.L. Hench, In situ spectroscopic study of nucleic acids in differentiating embryonic stem cells, Vib. Spectrosc. 35 (2004) 199–203, http://dx.doi.org/10.1016/j.vibspec.2004.01.014.

[51] H.P. Buschman, G. Deinum, J.T. Motz, M. Fitzmaurice, J.R. Kramer, A. van der Laarse, et al., Raman microspectroscopy of human coronary atherosclerosis: biochemical assessment of cellular and extracellular morphologic structures in situ, Cardiovasc. Pathol. 10 (2001) 69–82, http://dx.doi.org/10.1016/S1054-8807(01)00064-3.

[52] K.M. Marzec, A. Rygula, M. Gasior-Glogowska, K. Kochan, K. Czamara, K. Bulat, et al., Vascular diseases investigated ex vivo by using Raman, FT-IR and complementary methods, Pharmacol. Rep. 67 (2015) 744–750, http://dx.doi.org/10.1016/j.pharep.2015.05.001.

[53] M.B. Peres, L. Silveira, R.A. Zângaro, M.T.T. Pacheco, C.A. Pasqualucci, Classification model based on Raman spectra of selected morphological and biochemical tissue constituents for identification of atherosclerosis in human coronary arteries, Lasers Med. Sci. 26 (2011) 645–655, http://dx.doi.org/10.1007/s10103-011-0908-z.

[54] P. Sun, K.M. Dwyer, C.N. Merz, W. Sun, C.A. Johnson, A.M. Shircore, et al., Blood pressure, LDL cholesterol, and intima-media thickness: a test of the "response to injury" hypothesis of atherosclerosis, Arterioscler. Thromb. Vasc. Biol. 20 (2000) 2005–2010.

[55] V.M. Subbotin, Excessive intimal hyperplasia in human coronary arteries before intimal lipid depositions is the initiation of coronary atherosclerosis and constitutes a therapeutic target, Drug Discov. Today 21 (2016) 1578–1595, http://dx.doi.org/10.1016/j.drudis.2016.05.017.

[56] M. Jermyn, K. Mok, J. Mercier, J. Desroches, J. Pichette, K. Saint-Arnaud, et al., Intraoperative brain cancer detection with Raman spectroscopy in humans, Sci. Transl. Med. 7 (2015), http://dx.doi.org/10.1126/scitranslmed.aaa2384 (274ra19–274ra19).

[57] J. Wang, K. Lin, W. Zheng, K.Y. Ho, M. Teh, K.G. Yeoh, et al., Comparative study of the endoscope-based bevelled and volume fiber-optic Raman probes for optical diagnosis of gastric dysplasia in vivo at endoscopy, Anal. Bioanal. Chem. 407 (2015) 8303–8310, http://dx.doi.org/10.1007/s00216-015-8727-x.

[58] J.C.C. Day, N. Stone, A subcutaneous Raman needle probe, Appl. Spectrosc. 67 (2013) 349–354, http://dx.doi.org/10.1366/12-06651.

[59] A.P.M. Michel, S. Liakat, K. Bors, C.F. Gmachl, In vivo measurement of mid-infrared light scattering from human skin, Biomed. Opt. Express 4 (2013) 520, http://dx.doi.org/10.1364/BOE.4.000520.

[60] S. Perakis, M.R. Speicher, Emerging concepts in liquid biopsies, BMC Med. 15 (2017) 75, , http://dx.doi.org/10.1186/s12916-017-0840-6.